ELSEVIER

Nuclear Instruments and Methods in Physics Research A 403 (1998) 425–430

NUCLEAR INSTRUMENTS & METHODS IN PHYSICS RESEARCH Section A

Electrode thickness measurement of a Si(Li) detector for the SIXA array

T. Tikkanen[a,*], K. Hämäläinen[b], S. Huotari[b]

[a] *Observatory and Astrophysics Laboratory, P.O. Box 14 (Tähtitorninmäki), FIN-00014 University of Helsinki, Finland*
[b] *Department of Physics, P.O. Box 9, FIN-00014 University of Helsinki, Finland*

Received 10 October 1997

Abstract

Cathode electrodes of the Si(Li) detector elements of the SIXA X-ray spectrometer array are formed by gold–palladium alloy contact layers. The equivalent thickness of gold in one element was measured by observing the characteristic L-shell X-rays of gold excited by monochromatised synchrotron radiation with photon energies above the L_3 absorption edge of gold. The results obtained at four different photon energies below the L_2 edge yield an average value of 22.4 ± 3.5 nm which is consistent with the earlier result extracted from detection efficiency measurements.

PACS: 29.40.Wk; 85.30.De; 07.85.Nc; 95.55.Ka

Keywords: Si(Li) detectors; X-ray spectrometers; X-ray fluorescence; Detector calibration; Gold electrodes; Synchrotron radiation

1. Introduction

The SIXA (Silicon X-Ray Array) detector [1,2] is a focal plane instrument of the SODART X-ray telescope on board the Spectrum-X-Gamma satellite scheduled for launch in 1998. SIXA detects X-rays in the energy range between 500 eV and 20 keV with a closely packed array of 19 discrete Si(Li) detector elements. The elements are cylindrical and their active detection volume is 9.2 mm in diameter and 3.0 mm in thickness.

X-rays impinge on the detector through the cathode side of the Si(Li) crystals. The cathode consists of a contact layer manufactured by sputter deposition of gold–palladium alloy on the crystalline silicon. The Au/Pd mass ratio of the alloy is 60 : 40 and the nominal thickness is 30 nm but deviations from this value are expected to be large for the individual detectors because the Si(Li) crystals are batch processed to deposit the alloy. Knowledge of the individual Au/Pd thickness for each element in the array is necessary, since the electrode thickness is the dominant factor determining the detection efficiency in the lower part of the energy range.

The electrode thickness can be deduced from absolute measurements of the detection efficiency

* Corresponding author. Tel.: + 358 9 19122940; fax: + 358 9 19122952; e-mail: tuomo.tikkanen@helsinki.fi.

0168-9002/98/$19.00
PII S0168-9002(97)01152-2

at low energies. Such a measurement was carried out for one detector element using synchrotron radiation in the soft X-ray energy region from the electron storage ring BESSY, yielding a result of 40.7 nm [3]. However, in this case the windowless detector was operated in the beamline vacuum, which is not practically achievable for all SIXA elements which are assembled in a common capsule. Instead, the calibration of the flight detector array will be done with harder X-ray sources such as X-ray tubes and radioisotopes.

We used the method of Hansen et al. [4] to measure the gold thickness by detecting the gold L-shell fluorescence induced by primary X-rays of higher energy. In principle, the palladium thickness could be measured similarly using primary photon energies above the K edge of palladium, but this measurement would not be possible with the flight array because its data acquisition system has an upper limit of 20 keV. It has been noted that the fluorescence lines are spread into broad bands due to the escape of photoelectrons from the contact layer into the active detection volume [5] and an experimental correction for the resulting error was applied by Campbell and Wang [6]. We have modelled the full shape of the fluorescence lines, including the low-energy tails as well as the high-energy tail contributions from the escape of Auger electrons and photoelectrons. Primary photon energies above the L_1 absorption edge of gold were used in other reported measurements [7,5,8] but we also used energies between the L_3 and L_2 edges in order to eliminate the uncertainties from quantities related to the individual L subshells.

2. Experiment

Using the transfer standard SIXA detector element which has been characterised at BESSY in the energy range below 5 keV [3], we recorded energy spectra using monochromatised synchrotron radiation at the beamline X18B of the electron storage ring NSLS at the Brookhaven National Laboratory. The detector was operated at about 106 K in a cryostat sealed with an aluminium-coated polyimide window. In addition, an 8.5 μm thick beryllium window was used to suppress light.

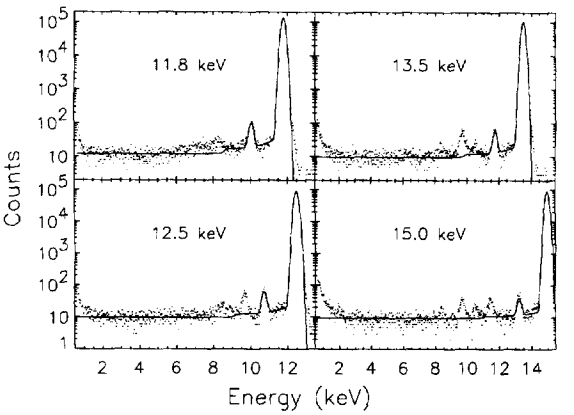

Fig. 1. Measured pulse height spectra of monochromatised X-rays at photon energies 11.8, 12.5, 13.5 and 15.0 keV. The curves show the calculated shape of the primary line including its low-energy tail.

The windows were transparent in a circular area having a diameter of 5.9 mm. Between the detector and the exit window of the beamline were an ionisation chamber and about 40 cm of air. We attenuated the beam by eight orders of magnitude in order to reach reasonable count rates of about 1000 s^{-1}. This was achieved by using two pinhole apertures.

Spectra were acquired first with the beam directed at the centre of the detector surface. A few examples are shown in Fig. 1 together with model functions of the primary peak including the low-energy tail extrapolated from the low-energy characterisation results. The gold Lα line was best resolvable at the photon energy of 12.5 keV and we used this energy when we recorded spectra with the beam directed at four different positions on the detector surface.

3. Fluorescence model

When the Si(Li) detector is irradiated with X-rays, the gold atoms in the contact layer emit characteristic photons isotropically into all directions. The detected fluorescence lines have more tailing than lines produced by normally incident primary radiation. High-energy tails are formed by events where the characteristic photon is accompanied

with an energetic electron escaping from the electrode into the active detection volume. Low-energy tails due to energy loss across the alloy/silicon interface are higher for isotropically incident radiation because absorption is more concentrated near the surface.

In the primary photon energy range of 11.919–13.734 keV between the L_3 and L_2 edges, $L\alpha_1$ is the strongest fluorescence line and Auger electrons have usually greater energies than photoelectrons. The most probable Auger electron to follow $L\alpha_1$ photon emission is $M_5N_5N_7$ (energy 1.79 keV). Its range in the Au/Pd alloy is $R_{Aug} = 21$ nm [9]. Assuming isotropic initial direction distribution of the Auger electrons, the fraction of Auger electrons generated within the distance $d \leqslant R_{Aug}$ from the alloy/silicon interface which will cross the interface is given by $p_{iso}(d/R_{Aug})$, where

$$p_{iso}(x) = \frac{1}{4}\arcsin x + \frac{1}{4}x\sqrt{1-x^2} - \frac{1}{6}(2x - x^2)^{3/2}. \tag{1}$$

For most if not all detector elements the electrode thickness T is greater than R_{Aug} and as the primary photons are absorbed very homogeneously throughout the whole thickness, the Auger electron escape probability is $P_{Aug} = (1 - \omega_{M_5})p_{iso}R_{Aug}/T$, where ω_{M_5} is the M_5-shell fluorescence yield and $p_{iso} \equiv p_{iso}(1) = \frac{\pi}{8} - \frac{1}{6}$. The photoelectron escape probability is obtained similarly: $P_{pho} = p_{pho}R_{pho}/T$, where $p_{pho} = 0.153$ [10] is the average escape probability of the photoelectrons generated within their range R_{pho} from the interface. Adding these and subtracting the probability of simultaneous escape of both electrons to prevent these events from being counted twice, the tail-to-total ratio for the high-energy tail is obtained as

$$P_h = P_{Aug} + P_{pho}(1 - P_{Aug}). \tag{2}$$

The components of the low-energy tail for isotropically incident radiation are obtained by integration over all directions. For the silicon escape peak the result is, neglecting escape through the sides and rear of the cylinder,

$$P_{esc} = \frac{1}{8}\omega_K f_K\left[1 - x\ln\left(1 + \frac{1}{x}\right) + \frac{1}{x}\ln(1 + x)\right], \tag{3}$$

where ω_K is the K-shell fluorescence yield of silicon, f_K is the fractional contribution of the K shell to μ (the linear attenuation coefficient of silicon at the primary photon energy) and $x = \mu_K/\mu$, where μ_K is the linear attenuation coefficient of silicon at the K line energy. The other components are derived from the physical model of Scholze and Ulm [10]. For the short tail, the integration yields

$$P_t = \frac{1}{2}\int_0^1 (1 - e^{-\mu R/x})\,dx, \tag{4}$$

where $R = 210$ nm is a parameter of the model. When calculating the escape of the primary electrons from silicon into the electrode, it is assumed that the photoelectrons are ejected isotropically into all directions because the absorbed photons arrive isotropically from the half-space. The resulting contribution to the flat shelf is

$$P_{Si} = \frac{1}{2}p_{iso}\int_0^1 (2 - e^{-\mu R_{pho}/x} - e^{-\mu R_{Aug}/x})\,dx. \tag{5}$$

The low-energy tail contributions are compared to those for normally incident radiation from an external source of the same energy in Table 1. The flat shelf contribution was calculated with $T = 40.7$ nm. The total fraction of counts in the low-energy tail is 1.8% while for normally incident radiation it is 0.7%.

When the primary beam is directed at the central region, all L-series characteristic photons emitted by gold atoms into the half-space formed by the Si(Li) bulk are detected and the full-peak absolute quantum detection efficiency for the characteristic line is

$$\varepsilon_{Au} = \frac{1}{2}(1 - A)(1 - P_h)(1 - P_{esc} - P_t - P_{Si}), \tag{6}$$

Table 1
Components of the low-energy tail of the Si(Li) detector for the $L\alpha_1$ characteristic line of gold: normally incident radiation (left column), fluorescence generated in the electrode (right column)

	External (%)	Electrode (%)
Si escape	0.10	0.16
Short tail	0.17	0.58
Flat shelf (Si)	0.10	0.41
Flat shelf (total)	0.46	1.01

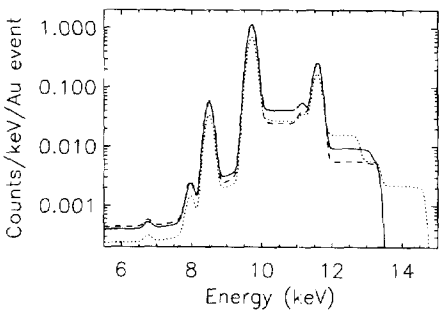

Fig. 2. Calculated pulse height spectra of X-ray fluorescence from the electrode with primary photon energies of 12.0 keV (dashed curve), 13.5 keV (solid curve) and 15.0 keV (dotted curve). The total count rate is normalised to the total rate of primary photon absorption events by gold atoms.

where A is the self-absorption probability in the electrode given by

$$A = 1 - \int_0^1 \frac{x}{\mu_{\mathrm{Au/Pd}} T}\left(1 - \mathrm{e}^{-\mu_{\mathrm{Au/Pd}} T/x}\right) \mathrm{d}x, \tag{7}$$

which yields 2.2% for the Lα line. With the approximation that the self-absorption events are uniformly distributed across the electrode thickness, the shelf contribution from the escape of primary electrons into the active detection volume is obtained as

$$P_{\mathrm{Au/Pd}} = \frac{A}{\mu_{\mathrm{Au}} + \mu_{\mathrm{Pd}}} \sum_{i=\mathrm{Au}}^{\mathrm{Pd}} \mu_i \times \left[p_{\mathrm{iso}} \left(\frac{T}{R_{\mathrm{pho},\,i}} \right) + p_{\mathrm{iso}} \frac{R_{\mathrm{Aug},\,i}}{T} \right], \tag{8}$$

since the applicable photoelectron ranges are now greater than T.

Calculated shapes of the fluorescence lines from L_3 shell ionisation are shown in Fig. 2, including $L\alpha_1$, $L\beta_{2,15}$, $L\alpha_2$, $L\iota$, $L\beta_5$ and $L\beta_6$. The electron ranges in Eqs. (2), (5) and (8) were calculated using the most probable Auger and photoelectron energies. The high-energy tail, being produced like the flat shelf by escape of energetic electrons, consists of two step functions convolved with a Gaussian, one due to the Auger electron and the other one to the photoelectron. For primary photon energies above the L_2 edge, a third one due to a Coster–Kronig electron is added.

When the primary photon energy E is between the ionisation energies of the L_3 and L_2 shells of gold, the intensity ratio of the Au Lα line and the primary line is given by

$$\frac{I_{\mathrm{Au}}}{I(E)} = \omega_{\mathrm{L_3}} f_{\mathrm{L}\alpha} \frac{\varepsilon_{\mathrm{Au}}}{\varepsilon(E)} \left(1 - \mathrm{e}^{-\mu_{\mathrm{L_3}}(E)t}\right), \tag{9}$$

where $\omega_{\mathrm{L_3}}$ is the fluorescence yield of the gold L_3 shell, $f_{\mathrm{L}\alpha}$ is the intensity ratio of Lα to all L_3-series lines, ε is the quantum detection efficiency of the Si(Li) detector, $\mu_{\mathrm{L_3}}$ is the L_3-shell linear attenuation coefficient of gold and t is the equivalent gold thickness. Above the L_2 and L_1 absorption edges the Lα line includes contributions from absorptions to the other L subshells followed by Coster–Kronig transitions. With the approximation $1 - \mathrm{e}^{-\mu t} \approx \mu t$ the thickness is given by

$$t = \left(\frac{I(E)}{I_{\mathrm{Au}}}\right)\left(\frac{1}{\omega_{\mathrm{L_3}} f_{\mathrm{L}\alpha}}\right) \frac{\varepsilon(E)}{\varepsilon_{\mathrm{Au}}\mu_{\mathrm{L_3}}(E) + f_{23}\varepsilon_{\mathrm{Au},\,2}\mu_{\mathrm{L_2}}(E) + (f_{13} + f_{12}f_{23})\varepsilon_{\mathrm{Au},\,1}\mu_{\mathrm{L_1}}(E)}, \tag{10}$$

where the f's are the applicable Coster–Kronig yields and $\varepsilon_{\mathrm{Au},2}$ and $\varepsilon_{\mathrm{Au},1}$ have different high-energy tails than $\varepsilon_{\mathrm{Au}}$ because the photoelectron energies are different and the escape of Coster–Kronig electrons add new tail contributions. Our calculation includes the high-energy tail contribution $P_{\mathrm{CK},2} = \frac{1}{2} f_{23} p_{\mathrm{iso}} R_{23}/T$ for $\varepsilon_{\mathrm{Au},2}$, where the factor $\frac{1}{2}$ represents roughly the probability that the Coster–Kronig electron is energetic (i.e. not of the LLM series) and R_{23} is the range of the $L_2L_3N_1$ Coster–Kronig electron. For $\varepsilon_{\mathrm{Au},1}$ we set $P_{\mathrm{CK},1} = f_{13} p_{\mathrm{iso}} R_{13}/T$. The contributions of the individual L subshells to μ were calculated from the jump ratios using the data of Henke et al. [11].

4. Results

Net counts in the gold fluorescence lines were calculated by fitting the modelled shape of the lines

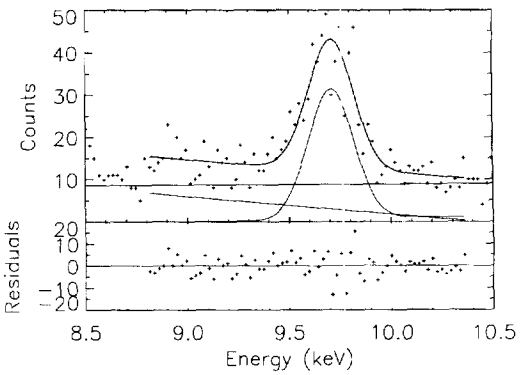

Fig. 3. Illustration of the data analysis at the primary photon energy of 13.0 keV: measured data (points) and the best-fit model function (curve) are shown in the upper panel and their difference in the energy region used in the fitting in the lower panel. The thin curves are the gold Lα fluorescence line and the added linear background component.

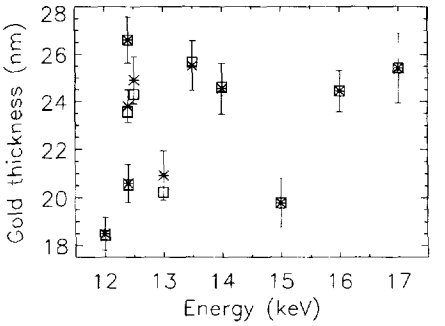

Fig. 4. Equivalent gold thickness calculated from data obtained using different primary photon energies. The error bars show the statistical 1σ uncertainties from the limited number of the gold Lα photons. Results using an alternative method to compute net counts (extrapolated low-energy model function for the tail of the primary peak) are indicated by squares. Off-centre results acquired at 12.5 keV are plotted at 12.4 keV for the sake of clarity.

plus continuum to the data in the region of the Lα peak. Ideally, the continuum is formed by the low-energy tail of the primary peak. However, the measured continua are higher than the modelled tails in certain energy regions (see Fig. 1). A broad feature above 8 keV appears in all spectra up to the primary photon energy of 13.0 keV, including the data taken at 11.8 keV which is below the L edges of gold. This feature can be a measurement artifact or reflect the real shape of the tail; our extrapolated tail model is based on a physical model which applies to photon energies below 4 keV [10]. At photon energies above 13.0 keV, the Lα line of lead at 10.5 keV appears. This line originates in lead impurities in the slits and apertures. The continuum might as well be modelled using the original form of the modified HYPERMET function [12,13]. We tried both forms and added a first-order polynomial to fit the unknown feature. The best-fit lead Lα lines were added to the continuum at photon energies above the L_3 absorption edge of lead. An example is shown in Fig. 3 (original form).

Fig. 4 presents the thicknesses obtained from Eq. (10), both using the original HYPERMET form and the form of Ref. [10]. Statistical uncertainties (standard deviation in the true photon number) were derived from the net counts in the Lα peak. Weighted average of the results from 12.0 to 13.5 keV at the detector centre is 22.4 nm with a standard deviation of 3.5 nm with the original form and 22.2 ± 3.5 nm with the other form. The 16% standard deviations are higher than the real uncertainty of the intensity. This is explained by the fluctuations of the continuum counts and by errors in the electron ranges, absorption coefficients and other data. Inclusion of the results up to 16.0 keV yields 22.8 ± 2.9 nm with the original form (results at 17.0 keV and above are excluded because the continuum is dominated by Compton scattering). The results at 12.5 keV at different positions yield an average of 23.9 nm with a standard deviation of 2.3 nm which means that thickness variations across the detector surface greater than the overall precision were not found.

5. Conclusions

The gold–palladium alloy contact layer thickness of a Si(Li) detector element for the SIXA array was measured using monochromatised synchrotron radiation to excite L-shell fluorescence from gold. The fluctuation of the result as function of

primary photon energy yields an accuracy of about 3 nm in the equivalent thickness of gold. The result is in agreement with an earlier result 20.1 ± 0.3 nm derived from a detection efficiency measurement [3]. The contact layer thicknesses of the elements in the SIXA flight array are to be measured using monochromatised radiation of an X-ray tube with longer acquisition times which will reduce the uncertainty from photon statistics. The accuracy will be limited by the knowledge of the shape of the low-energy tail of the primary peak and the uncertainty in the electron ranges and the absorption coefficients and other data regarding the L subshells of gold.

Acknowledgements

We thank L. Furenlid of the Brookhaven National Laboratory for collaboration at the beamline and Metorex International Oy (Espoo, Finland) for providing the detector. S. Kraft of the Physikalisch-Technische Bundesanstalt, Berlin, is acknowledged for extrapolating the HYPERMET function parameters to the higher part of our energy range. This work was supported by the Academy of Finland (contract SA-8582).

References

[1] O. Vilhu, J. Huovelin, T. Tikkanen, P. Hakala, P. Muhli, V.J. Kämäräinen, H. Sipilä, I. Taylor, J. Pohjonen, H. Päivike, J. Toivanen, R. Sunyaev, A. Kuznetsov, A. Abrosimov, Proc. SPIE 2279 (1994) 532.
[2] O. Vilhu, J. Huovelin, T. Tikkanen, P. Hakala, P. Muhli, V.J. Kämäräinen, H. Sipilä, I. Taylor, J. Pohjonen, H. Päivike, J. Toivanen, R. Sunyaev, A. Kuznetsov, A. Abrosimov, Nordic Conference on Theoretical High Energy Astrophysics, Copenhagen, 14–16 September, 1997 (proceedings to be published in Physica Scripta).
[3] T. Tikkanen, S. Kraft, F. Scholze, R. Thornagel, G. Ulm, Nucl. Instr. and Meth. A 390 (1997) 329.
[4] J.H. Hansen, J.D. McGeorge, D. Nix, W.D. Schmidt-Ott, I. Uns, R.W. Fink, Nucl. Instr. and Meth. 106 (1973) 365.
[5] W. Maenhaut, H. Raemdonck, Nucl. Instr. and Meth. B 1 (1984) 123.
[6] J.L. Campbell, J.-X. Wang, X-ray Spectrom. 20 (1991) 191.
[7] K. Shima, K. Umetani, T. Mikumo, J. Appl. Phys. 51 (1980) 846.
[8] J.L. Campbell, P.L. McGhee, Nucl. Instr. and Meth. A 248 (1986) 393.
[9] H.-J. Fitting, Phys. Status Solidi (a) 26 (1974) 525.
[10] F. Scholze, G. Ulm, Nucl. Instr. and Meth. A 339 (1994) 49.
[11] B.L. Henke, E.M. Gullikson, J.C. Davis, Atom. Data and Nucl. Data Tables 54 (1993) 181.
[12] G.W. Phillips, K.W. Marlow, Nucl. Instr. and Meth. 137 (1976) 525.
[13] J.L. Campbell, B.M. Millman, J.A. Maxwell, A. Perujo, W.J. Teesdale, Nucl. Instr. and Meth. B 9 (1985) 71.